

The Dynamics of the Solar Interior

Toby Wood

January 21, 2008

Abstract

Until the 1960s, observational data concerning the Sun's rotation was restricted to line-of-sight observations of the solar surface. The Sun was seen to have significant differential rotation, the surface angular velocity increasing by about 30% from pole to equator. Later, helioseismology revealed that this differential rotation persists down to the base of the convection zone, at around $0.7R_{\odot}$, but that the radiation zone beneath rotates uniformly, at a rate equal to that of the convection zone at around 35° latitude. The transition between these two zones takes place over a thin layer known as the 'tachocline'. In this paper we follow up the suggestion of Gough & McIntyre [15] that the uniform rotation of the Sun's radiation zone can only be explained by the presence of a large-scale magnetic field, which must be prevented from diffusing into the overlying high-latitude convection zone by meridional circulations within the intervening tachocline. We derive boundary layer equations for this 'magnetic confinement problem' in the polar regions of the tachocline, and obtain similarity solutions valid over some range of latitudes. For an internal field of strength $\lesssim 2000\text{G}$, these solutions could apply as far as 40° latitude, covering the entire latitude range over which the convection zone rotates slower than the radiation zone.

Declaration

The work contained in this essay was carried out by myself, in collaboration with my supervisor Prof. Michael McIntyre, unless otherwise stated. §1–8 constitute a review of relevant background material; §9–13 represent new material. §9.5–9.8 are based on [37], a 6 page paper written by myself and Michael McIntyre.

§A derives many of the basic results used in earlier sections and is not original research, with the following exceptions:

- §A.3.2 examines the same problem as described in Haynes et al. [16], but takes a rather different approach, seeking appropriate boundary conditions by a generalised energy method.
- §A.4 re-derives a particular case of Tayler instability found by Spruit [33] from Acheson's dispersion relation [1]. However, the instability is here derived directly from the Boussinesq MHD equations in cylindrical polar coordinates, valid for arbitrarily small colatitudes. Acheson's dispersion relation was derived from a local plane wave assumption and the non-Boussinesq equations.

T.S. Wood.....

M.E. McIntyre.....

Contents

1	The Sun’s Rotation	3
2	Spindown by Meridional Circulations	3
3	Non-uniform Rotation	4
4	Helioseismology	4
5	The Tachocline	5
6	Horizontal Hydrodynamic Turbulence	6
7	The Sun’s Internal Magnetic Field	6
8	Magnetic Confinement	7
9	The Magnetic Confinement Layer	9
9.1	Modelling assumptions	9
9.2	Equations	9
9.3	The Tachopause	11
9.4	Boundary Conditions	11
9.5	The Leading Order Solution	12
9.6	Properties of the Solutions	14
9.7	Scale Analysis	15
9.7.1	Rossby Number, \mathcal{R}	16
9.7.2	Radius of validity	16
9.7.3	Richardson Number, Ri_η	16
9.7.4	Taylor instability	17
9.8	Possible Parameter Ranges	17
10	The Tachopause	18
11	The Tayler–Spruit Scenario	18
12	Concluding Remarks	20
13	Future Work	20
14	Acknowledgements	20
A	Appendix	21
A.1	Parameter Values	21
A.2	The Perfect Gas Equations	21
A.2.1	The Taylor–Proudman Theorem	21
A.2.2	Thermal Wind	21
A.3	Meridional Circulation and Spindown	22
A.3.1	Gyroscopic pumping	22
A.3.2	Downward control	22
A.3.3	The hydrodynamic tachocline model	24
A.4	The Tayler Instability	25
A.5	The Tayler–Spruit Dynamo	26

1 The Sun’s Rotation

The gas cloud from which the Sun formed would have had around 10^5 times the angular momentum of the present Sun [14]. Though the mechanisms controlling angular momentum loss in a pre-main sequence star are in dispute, the spindown of a main sequence star is better understood. On scales for which magnetic diffusion is negligible, ideal (i.e. diffusionless) MHD predicts that the magnetic field is materially advected by the flow — this is Alfvén’s Theorem. The material continually escaping the Sun in the pseudo-steady solar wind therefore follows the path described by the Sun’s external magnetic field lines. Close to the surface of the Sun, where the outward propagation of Alfvén waves along the field lines is faster than the solar wind speed, the Lorentz force from the Sun’s field constrains the accelerating solar wind to corotate with the Sun’s surface. This corotation persists out to the Alfvén radius ($\approx 20R_\odot$), where the solar wind overtakes the Alfvén waves, and thus overcomes the ‘rigidity’ of the field lines. This extended region of corotation produces a ‘magnetic lever arm’ that greatly enhances the spindown of the solar surface. However, the ‘magnetic braking’ does not extend beneath the solar surface, where the assumption of a pseudo-steady magnetic field breaks down. Understanding how the surface spindown is transmitted to the Sun’s underlying convection zone, and further into the interior, requires a review of spindown in general, and in particular the role of meridional circulations.

2 Spindown by Meridional Circulations

In any rotating fluid, a persistent retrograde force leads to spindown. The individual fluid particles that are subject to the force drift toward the rotation axis in a manner analogous to the orbital decay of satellites, and to the inward drift of dust in a protoplanetary accretion disk. This process has been called ‘gyroscopic pumping’ because of its dependence on Coriolis effects (see §A.3.1). In a fluid, this persistent pumping leads to a meridional circulation, as demanded by mass conservation. A famous example of such a flow occurs in the experiment known as ‘Einstein’s tea leaves’: spindown within a stirred cup of tea is driven by a viscous retrograde force exerted on the fluid by the base of the cup [8]. This persistent retrograde force gyroscopically pumps fluid toward the rotation axis within a thin Ekman layer at the base of the cup (see Figure 1a). Recirculation occurs throughout the rest of the fluid, leading to spindown via the ‘anti-ballerina’ effect. As long as the cup is sufficiently large that the global viscous diffusion time is longer than the rotation period, this is the dominant mechanism producing spindown.

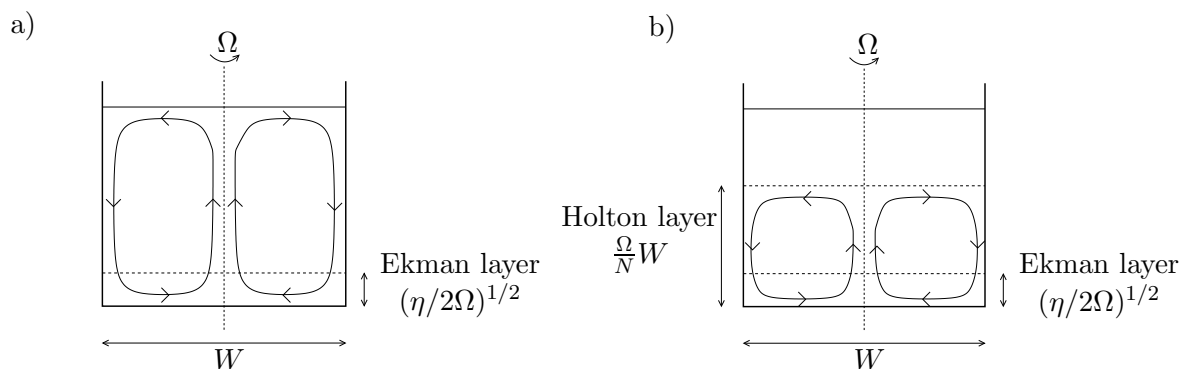


Figure 1: Spindown in a tea cup is driven by an Ekman layer at the base. a) Without stratification; b) With stratification, buoyancy frequency N .

If we consider a variation on the tea leaves problem in which the fluid is strongly stratified, then the spindown circulation is confined to a Holton layer [17] whose aspect ratio is approximately the ratio of buoyancy and rotation frequencies (see Figure 1b). Within this layer, the ‘Taylor–Proudman effect’ is able to overcome the stratification constraint and dominate the dynamics (see §A.2.1). An analogous model describing solar spindown was formulated by Spiegel [31]. They described how turbulent stresses within the Sun’s convection zone could drive ‘spindown currents’ within a thin layer at the top of the stably stratified radiation zone beneath; he called this layer the ‘tachycline’ (see Figure 2).

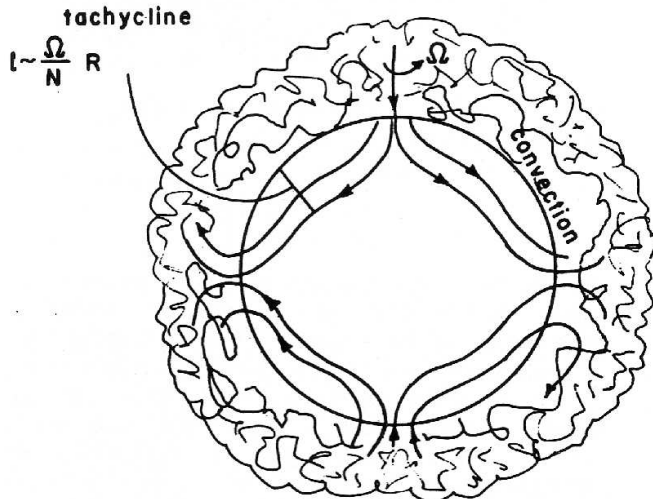


Figure 2: Spindown currents within a nonmagnetic ‘tachycline’, taken from [31].

If we now allow for thermal diffusivity, then weak currents can break the stratification constraint and spread further into the fluid. This is sometimes known as ‘radiative spreading’ and causes the effects of spindown to spread at a rate given by the local Eddington–Sweet time (see §A.3.3). An example of this process takes place within the Earth’s stratosphere, where breaking Rossby and gravity waves produce a mean azimuthal forcing that pumps fluid poleward. Though the forcing varies in both space and time, when suitably averaged it is seen to drive a mean meridional circulation (MMC). In the absence of impenetrable barriers, the return flow of this circulation occurs *beneath* the forcing layer - this phenomenon is called ‘downward control’ (see §A.3.2). We may then describe the spreading of these spindown currents as ‘burrowing’ into the denser material beneath.

So the magnetic braking of the solar surface must also drive a meridional circulation within the convection zone [29], and indeed a mean meridional flow can be observed in the surface motions. The average flow speed is around 300cm s^{-1} , and therefore takes approximately one year to travel from equator to pole [26].

3 Non-uniform Rotation

Another variation of the spindown problem is to consider the effect of imposing a particular rotation profile, at some fixed altitude, within a fluid initially in uniform rotation. This can be achieved either through an inhomogeneous boundary condition or the application of an appropriate volume force. In the case of a cup of unstratified tea, we expect the Coriolis force to come into balance with the horizontal pressure gradient, so that the angular velocity contours become vertical, in accordance with the Taylor–Proudman theorem (see §A.2.1). However, the shape of the contours is modified in the presence of baroclinicity. In particular, strong stratification can dominate over the rotation. The Taylor–Proudman theorem then only holds over a shallow region, as in the case of the Holton layer described earlier.

4 Helioseismology

In the 1970s, it became possible to infer some of the Sun’s internal properties through helioseismology. In particular, differential rotation leads to frequency splitting of acoustic p -modes, which may be detected in the surface oscillations. Thus it was found that the pattern of differential rotation at the Sun’s surface persists down to the bottom of the convection zone ($\approx 0.7R_{\odot}$). The angular velocity contours are inclined to the rotation axis at an angle close to 30° , contradicting the Taylor–Proudman theorem and demonstrating the importance of baroclinicity (see Figure 3). More surprisingly, the rotation becomes uniform in the radiation zone beneath $0.7R_{\odot}$; the angular velocity in this region is roughly that of the convection zone at latitude 35° . The transition to uniform rotation takes place across a layer

too thin to be resolved by helioseismology, but estimated to be only $0.05R_{\odot}$. This layer is called the *tachocline*.

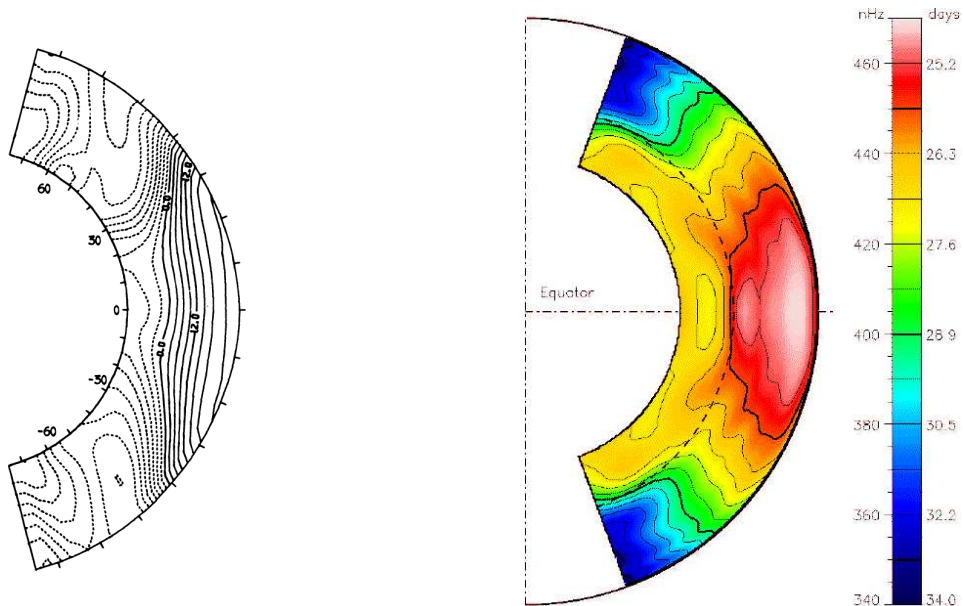


Figure 3: The convection zone’s angular velocity contours. The left plot shows the numerical model of Gilman & Miller [12], which has contours aligned with the rotation axis. The right plot shows the real Sun, as inferred from helioseismology, with ‘conical’ contours inclined at about 30° to the rotation axis.

5 The Tachocline

At first sight, the tachocline is reminiscent of the ‘tachycline’ described in Spiegel’s model of solar spindown — in fact this is the origin of its name. However, the tachycline regime is purely transient, since the overlying rotation profile burrows downward on the local Eddington–Sweet timescale. Spiegel & Zahn [32] showed that, in a purely laminar, hydrodynamic model, a tachocline layer of negligible initial thickness would burrow down beneath $0.5R_{\odot}$ over the Sun’s present main sequence lifetime (see §A.3.3). Nevertheless, strong dynamical coupling between the radiation and convection zones is still in evidence, since both exhibit the same mean rotation rate. So there must be some dynamical mechanism that holds the Sun’s radiative interior in uniform rotation even as it undergoes spindown. In particular, this mechanism must prevent the mean meridional circulations (MMCs) that spin down the convection zone from burrowing into the radiation zone. Two potential candidates for this mechanism, horizontal hydrodynamic turbulence and an interior magnetic field, are discussed in §6 and §7.

Magnetic braking at the solar surface is not the only retrograde force that pumps MMCs within the Sun: due to the persistent differential rotation observed in the convection zone and tachocline, any process that opposes this shear will drive such a circulation. We return to the issue of what drives the tachocline circulation in §11.

To fully describe the dynamics of the solar interior, we need to explain not only why the radiation zone continues to rotate uniformly but also why the convection zone ‘wants’ to rotate differentially. However, this second question is less controversial, since numerical simulations have been able to reproduce a convection zone with differential rotation of the same order as is observed by helioseismology. This ‘anti-frictional’ behaviour is attributed to anisotropic turbulent correlations between the largest plumes within the convection zone [4], though the underlying physical mechanism might be angular momentum flux transport by epicyclic waves [21]. Early numerical simulations tended to show angular momentum contours closely aligned with the rotation axis (see Figure 3), though the results proved to be dependent on the precise choice of boundary conditions. To reproduce the 30° slope of angular momentum contours observed in the Sun, Miesch, Brun & Toomre imposed a latitudinal temperature variation across the tachocline of around 10°K [25]. Although this suggests that the tachocline has some

dynamical back reaction onto the convection zone, the latitudinal differential rotation of the convection zone can still be taken as an imposed boundary condition on the tachocline to leading order, as was the case in Spiegel & Zahn’s analysis.

6 Horizontal Hydrodynamic Turbulence

Having noted the tachocline’s propensity to burrow downwards into a laminar, hydrodynamic interior, Spiegel & Zahn [32] went on to describe a process that might counteract this. They proposed that shear-driven turbulence, constrained by the tachocline’s stratification to be nearly horizontal, could act like an anisotropic viscosity, leading to enhanced horizontal dissipation of angular momentum. If this dissipation were sufficiently strong, it could homogenise the convection zone’s rotation profile over a layer the thickness of the tachocline, stopping the burrowing.

However, stably stratified, shear-driven turbulence has been studied in detail in a terrestrial context [20], where it is found to behave rather unlike local dissipation. Instead, the result is azimuthal homogenisation of potential vorticity and long-range latitudinal redistribution of angular momentum by waves [21]. This process typically drives the system in question *away* from solid rotation. The effect of such turbulence within a nonmagnetic solar interior would probably be analogous. For this reason, Gough & McIntyre [15] have argued that no purely hydrodynamic model can explain the Sun’s interior rotation.

7 The Sun’s Internal Magnetic Field

It is not currently possible to measure the magnetic field beneath the solar surface, although it is generally accepted that structurally stable field configurations must have comparable poloidal and toroidal components [27]. If the Sun’s interior has been in uniform rotation, and free from dynamo action, throughout its main-sequence history, then ohmic decay will have produced a poloidal component that is principally dipolar. Some insight into the likely configuration can be obtained from the numerical model of Braithwaite & Spruit, designed to simulate conditions inside Ap-type stars [2]. Their model predicts a roughly dipolar poloidal field, stabilised by a toroidal core (see Figure 4).

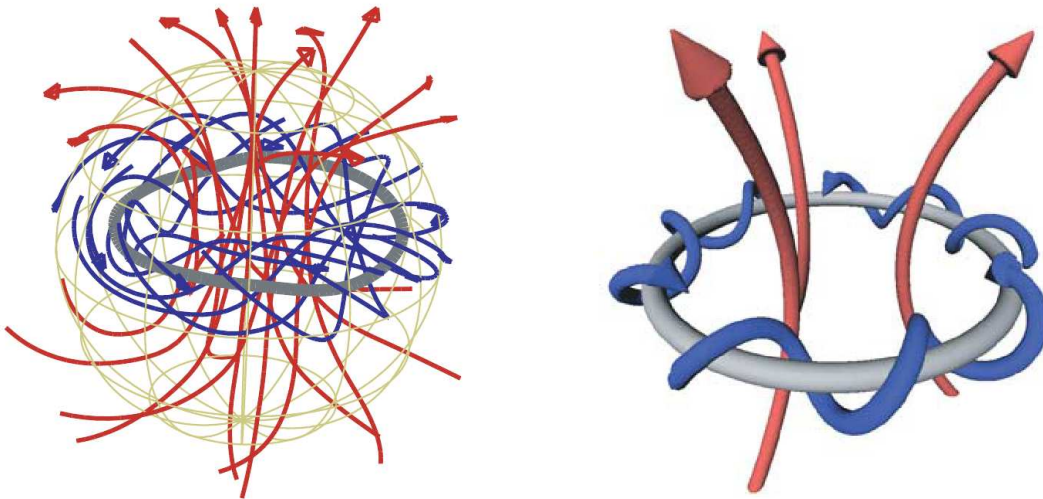


Figure 4: Numerical simulation of the internal field of an Ap star on the main sequence [2]. The field is roughly a dipole (red field lines) stabilised by a core of toroidal field (blue field lines). The right frame shows a simplified schematic.

If the Sun’s radiation zone harbours a similar magnetic field, this could explain why the convection zone’s differential rotation profile has not burrowed beneath the tachocline. The ability of large-scale magnetic fields to hold fluids in uniform rotation is well known. In ideal MHD, a steadily rotating system necessarily has constant angular velocity along each field line, i.e. if $\mathbf{u} = \Omega \mathbf{e}_z \times \mathbf{r}$ then $\mathbf{B} \cdot \nabla \Omega = 0$.

This is Ferraro’s Law of Isorotation [9] and is a special case of Alfvén’s Theorem. Shear disturbances to this uniform rotation generate Alfvén waves, leading to a torsional oscillation of the field with a period determined by the Alfvén travel time across the disturbance [35]. Though interactions between different oscillation modes are weak, for a sufficiently strong field the oscillation periods are short enough to produce significant destructive interference between modes on the timescale of solar evolution [7]. Studies by several authors, e.g. [24], [30] & [18], suggest that a poloidal field of only 10^{-2}G (with global Alfvén travel time $\approx 10^6$ years) would be sufficient to bring the Sun’s interior into uniform rotation¹. For the sake of mathematical simplicity, these studies all focus on the case of a magnetic field that is symmetric about the rotation axis; we shall make the same idealisation throughout this essay. If the Sun’s differential rotation predates its internal field, such that an initially weak field was wound up by differential rotation, then the resulting field configuration would be predominantly axisymmetric. This result, known as ‘rotational smoothing’, would apply in the solar case for an initial field $\lesssim 30\text{G}$ [28, 33].

8 Magnetic Confinement

If we suppose that the Sun’s radiation zone has a strong magnetic field that holds it in uniform rotation, we next need to explain what mechanism keeps the field confined to that zone. If the field were allowed to cross the tachocline, the differential rotation of the lower convection zone would be transferred to the interior, in accordance with the Ferraro constraint and contrary to the helioseismic evidence [18]. So the field must be confined (i.e. reduced to zero) across the tachocline, a problem previously addressed by Garaud, e.g. [10]. More recently, Brun & Zahn [5] showed that, even if the field is initially confined within the radiation zone, unchecked magnetic diffusion can cause the field lines to protrude into the convection zone, with the same result (see Figure 5). However, as is typical in such numerical simulations, their diffusivities are unrealistically large, exaggerating the rate at which this process occurs.

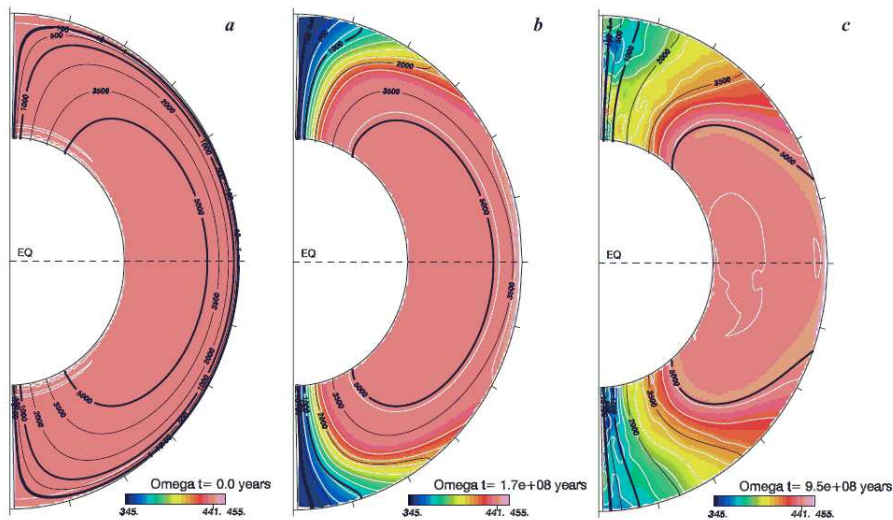


Figure 5: If the internal magnetic field is allowed to diffuse across the tachocline, the convection zone’s pattern of rotation becomes imprinted on the interior [5].

Gough & McIntyre proposed a model in which there is a two-way balance between the interior field and the mean meridional circulations (MMCs) of the convection zone: whilst the field prevents the meridional circulations from entering the interior, so the circulations themselves advect the field against ohmic diffusion. The magnetic confinement problem is most critical close to the poles, where some field lines must inevitably poke through to the convection zone, yet this is also where the vertical rotation gradient is largest. In these regions MMCs represent downwelling, an inward flow that holds the field in advection–diffusion balance across a thin *magnetic confinement layer* at the bottom of the

¹The arguments presented here do not rule out the possibility of material flowing *along* the magnetic field lines, as occurs in the solar wind. However, such flows are ‘choked’ by the strong stable stratification present in the radiation zone; we return to this point in later sections.

tachocline. Within this layer, all components of the magnetic field \mathbf{B} decay exponentially with height. The flow is prevented from entering the radiation zone by the Lorentz force from the confined field lines, which pushes the fluid equatorward. A possible field configuration near the north pole is illustrated in Figure 6.

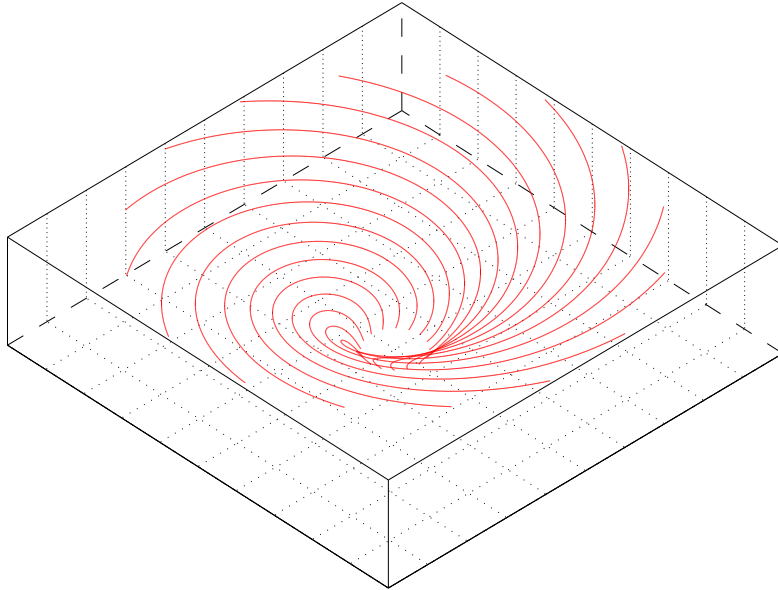


Figure 6: Magnetic field lines within the magnetic confinement layer around the north pole. This is the same solution as in Figures 7 & 8 later.

The Gough & McIntyre model consists of two regions:

- In the upper tachocline, the Taylor–Proudman effect leads to tilting of the stratification surfaces — the so-called ‘thermal wind balance’ (see §A.2.2). Thermal diffusion of the temperature anomaly is held in check by the vertical component of the MMC.
- In the magnetic confinement layer, the Lorentz force from the confined field lines pushes the flow equatorward, while the differential rotation ‘winds up’ the poloidal field, producing a strong toroidal component.

These statements describe the principal balances in the equations, though a complete scale analysis requires further assumptions to be made [11]. However, the vertical scale of the confinement layer, δ , is determined simply by the magnitude of the downwelling U into the layer via advection–diffusion balance: $\delta \sim \eta/U$, where the magnetic diffusivity² $\eta \approx 400\text{cm}^2\text{s}^{-1}$. To confine the field within a layer a few Mm thick, the downwelling therefore need only be around 10^{-5}cm s^{-1} .

Within the confinement layer, the persistent MMC provides efficient ‘ventilation’, keeping the chemical composition homogeneous with the rest of the tachocline. Within the stagnant radiation zone, however, gravitational settling produces a helium settling layer just beneath the tachocline, characterised by a vertical gradient in the mean molecular weight μ . Such a helium layer is a standard feature of solar models (e.g. [6]) and contributes significantly to the total stratification in that region. Following McIntyre [22], we suppose that this layer holds the base of the tachocline — the ‘tachopause’ — very close to horizontal (see [22, §8.5]). Due to the low self-diffusivity of helium ($\chi \approx 10\text{cm}^2\text{s}^{-1}$), the tachopause is virtually impenetrable to MMCs; this effect was described by Mestel & Moss as ‘ μ -choke’ [23]. The tachopause therefore marks a sharp discontinuity between the dynamic tachocline and the stagnant radiation zone. In §10 we describe how this discontinuity is resolved across a double boundary layer at the tachopause, and confirm that the layer is both thin and flat on the length scales characterising the magnetic confinement layer.

²All tachocline parameter values used are taken from [14] and listed in §A.1.

9 The Magnetic Confinement Layer

9.1 Modelling assumptions

The confinement layer is a thin, rotating, stably stratified layer of fluid at the bottom of the tachocline. The typical sound speed within this region, $c \approx 10^7 \text{ cm s}^{-1}$, is much faster than both the dynamical flows being considered and typical Alfvén speeds. This motivates us to make the anelastic approximation, which is widely employed in models of the solar interior [13]. We also note that the characteristic density and pressure scale heights ($H_\rho, H_p \approx 0.1R_\odot$) are greater than the thickness of the tachocline ($0.05R_\odot \approx 35 \text{ Mm}$). This allows us to adopt the Boussinesq approximation.

We shall assume that the confinement-layer flow is laminar (i.e. non-turbulent), so all diffusion coefficients take their microscopic values. We shall show later that viscosity only becomes significant in a very thin Ekman layer at the tachopause, and therefore neglect viscosity completely at this stage.

Finally, we shall assume that inertial effects are dominated by the Coriolis force, i.e. we neglect quadratic velocity terms in the rotating frame. This is justified provided the Rossby number \mathcal{R} remains small, which we shall confirm in §9.7.1. The problem remains nonlinear through the Lorentz force and the remaining advection terms.

9.2 Equations

We are principally concerned with the near-polar regions, where the confinement issue is most critical. We therefore adopt cylindrical polar coordinates to model the region around the north pole and work in the frame rotating with angular velocity $\boldsymbol{\Omega} = \Omega \mathbf{e}_z$, chosen to match the interior's uniform rotation. Since the Sun's angular momentum contours are very close to horizontal in high latitudes (see Figure 3), a cylindrical tachocline model is appropriate for this region. We then identify the (flat) tachopause with the plane $z = 0$. Finally, we take gravity to act in the vertical direction, $\mathbf{g} = -g\mathbf{e}_z$. Our equations are

$$\frac{\partial \mathbf{u}}{\partial t} + 2\boldsymbol{\Omega} \times \mathbf{u} = -\frac{c^2}{\gamma} \nabla \tilde{p} - \tilde{T} \mathbf{g} + (\nabla \times \mathbf{B}) \times \mathbf{B} \quad (1)$$

$$\nabla \cdot \mathbf{u} = 0 \quad (2)$$

$$\frac{\partial \mathbf{B}}{\partial t} = \nabla \times (\mathbf{u} \times \mathbf{B} - \eta \nabla \times \mathbf{B}) \quad (3)$$

$$\nabla \cdot \mathbf{B} = 0 \quad (4)$$

$$\frac{D\tilde{T}}{Dt} + \frac{N^2}{g} u_z = \kappa \nabla^2 \tilde{T} \quad (5)$$

where \tilde{p} and \tilde{T} are the relative perturbations of pressure and temperature to their hydrostatic background values. The sound speed c , adiabatic index γ and buoyancy frequency N are all constant, in accordance with the Boussinesq approximation. Both magnetic diffusivity η and thermal diffusivity κ take their constant, microscopic values, and we have chosen to measure the magnetic field \mathbf{B} in units of Alfvén velocity ($1 \text{ cm s}^{-1} \leftrightarrow 2 \text{ G}$ at tachocline mass densities).

We seek steady, axisymmetric solutions of these equations. We may therefore decompose the magnetic field into poloidal and toroidal components, where the poloidal part, \mathbf{B}_p , is given by the curl of some axisymmetric toroidal vector potential,

$$\mathbf{B}_p = \nabla \times (A_\phi \mathbf{e}_\phi). \quad (6)$$

The toroidal and poloidal parts of (3) are then, respectively,

$$0 = r \mathbf{B}_p \cdot \nabla \left(\frac{u_\phi}{r} \right) - r \mathbf{u}_p \cdot \nabla \left(\frac{B_\phi}{r} \right) + \eta \left(\nabla^2 - \frac{1}{r^2} \right) B_\phi \quad (7)$$

$$0 = \nabla \times (\mathbf{u}_p \times \mathbf{B}_p - \eta \nabla \times \mathbf{B}_p) \quad (8)$$

where r is the distance to the rotation axis. Since all non-zero, curl-free, toroidal vector fields are singular at the axis, we deduce from (8) that

$$0 = \mathbf{u}_p \times \mathbf{B}_p - \eta \nabla \times \mathbf{B}_p \quad (9)$$

$$\Rightarrow 0 = -\frac{1}{r} \mathbf{u}_p \cdot \nabla (r A_\phi) + \eta (\nabla^2 - \frac{1}{r^2}) A_\phi \quad (10)$$

We can eliminate the pressure perturbation by taking the toroidal parts of both (1) and its curl, which are

$$2\Omega u_r = \frac{1}{r} \mathbf{B}_p \cdot \nabla (r B_\phi) \quad (11)$$

$$2\Omega \frac{\partial u_\phi}{\partial z} = g \frac{\partial \tilde{T}}{\partial r} + \frac{1}{r} \frac{\partial}{\partial z} (B_\phi^2) + r \mathbf{B}_p \cdot \nabla \left[\frac{1}{r} (\nabla^2 - \frac{1}{r^2}) A_\phi \right] \quad (12)$$

If U is a measure of the typical fluid velocity within the system, then the characteristic length scale will be the magnetic advection–diffusion length, η/U . We therefore non-dimensionalise all velocity components with U and all lengths with respect to η/U . If we also non-dimensionalise the magnetic field components with $(\Omega\eta)^{1/2}$ and the temperature perturbation with $\frac{N^2\eta^2}{g\kappa U}$ then our equations become

$$2 \frac{\partial u_\phi}{\partial z} = \frac{1}{\epsilon^2} \frac{\partial \tilde{T}}{\partial r} + \frac{1}{r} \frac{\partial}{\partial z} (B_\phi^2) + r \mathbf{B}_p \cdot \nabla \left[\frac{1}{r} (\nabla^2 - \frac{1}{r^2}) A_\phi \right] \quad (13)$$

$$2u_r = \frac{1}{r} \mathbf{B}_p \cdot \nabla (r B_\phi) \quad (14)$$

$$\nabla \cdot \mathbf{u}_p = 0 \quad (15)$$

$$0 = -\frac{1}{r} \mathbf{u}_p \cdot \nabla (r A_\phi) + (\nabla^2 - \frac{1}{r^2}) A_\phi \quad (16)$$

$$0 = r \mathbf{B}_p \cdot \nabla \left(\frac{u_\phi}{r} \right) - r \mathbf{u}_p \cdot \nabla \left(\frac{B_\phi}{r} \right) + (\nabla^2 - \frac{1}{r^2}) B_\phi \quad (17)$$

$$\mathbf{B}_p = \nabla \times (A_\phi \mathbf{e}_\phi) \quad (18)$$

$$\frac{\eta}{\kappa} \mathbf{u}_p \cdot \nabla \tilde{T} + u_z = \nabla^2 \tilde{T} \quad (19)$$

where the dimensionless parameter ϵ is defined as

$$\epsilon^2 = \frac{\Omega \kappa U^2}{N^2 \eta^2}. \quad (20)$$

We first note that, within the tachocline, the Roberts number $\kappa/\eta \approx 3 \times 10^4$, so that the first term in (19) may be neglected. As noted previously, we anticipate that the downwelling into the top of the confinement layer will be of the order $10^{-5} \text{ cm s}^{-1}$, so $\epsilon \approx 10^{-4}$. This implies that thermal wind balance can be achieved in equation (13) with little tilting of the stratification surfaces; the problem has a ‘natural’ aspect ratio of $1/\epsilon$, corresponding to a ‘Margules slope’ of $O(\epsilon)$ (see §A.2.2). In fact, for $U \approx 10^{-5} \text{ cm s}^{-1}$, the vertical and horizontal scales are $\delta \approx 0.4 \text{ Mm}$ and $\delta/\epsilon \approx 2000 \text{ Mm}$, roughly comparable to the scalings for the high-latitude tachocline seen in helioseismic data. We therefore rescale all horizontal length scales and vector field components by a factor of $1/\epsilon$ and make the ‘thin layer’

approximation of neglecting horizontal diffusion. Thus we arrive at the set of dimensionless equations

$$2\frac{\partial u_\phi}{\partial z} = \frac{\partial \tilde{T}}{\partial r} + \frac{1}{r}\frac{\partial}{\partial z}(B_\phi^2) + r\mathbf{B}_p \cdot \nabla \left[\frac{1}{r}\frac{\partial^2}{\partial z^2}A_\phi \right] \quad (21)$$

$$2u_r = \frac{1}{r}\mathbf{B}_p \cdot \nabla(rB_\phi) \quad (22)$$

$$\nabla \cdot \mathbf{u}_p = 0 \quad (23)$$

$$0 = -\frac{1}{r}\mathbf{u}_p \cdot \nabla(rA_\phi) + \frac{\partial^2}{\partial z^2}A_\phi \quad (24)$$

$$0 = r\mathbf{B}_p \cdot \nabla\left(\frac{u_\phi}{r}\right) - r\mathbf{u}_p \cdot \nabla\left(\frac{B_\phi}{r}\right) + \frac{\partial^2}{\partial z^2}B_\phi \quad (25)$$

$$\mathbf{B}_p = \nabla \times (A_\phi \mathbf{e}_\phi) \quad (26)$$

$$u_z = \frac{\partial^2 \tilde{T}}{\partial z^2} \quad (27)$$

9.3 The Tachopause

In our inviscid model, there must be a discontinuity in the horizontal velocity components at the sharp tachopause, and we see from (23–26) that this ‘slip flow’ produces a kink (i.e. a slope discontinuity) in the magnetic field lines. However, the Coriolis and Maxwell torques must remain in balance between the confinement layer and the uniformly rotating interior, so we deduce from (22) a relation between the velocity components immediately above the tachopause. Written in terms of dimensional quantities, this is

$$u_r = -\Lambda u_\phi \quad \text{at } z = 0^+, \quad (28)$$

where Λ is the Elsasser number

$$\Lambda \equiv \left. \frac{B_z^2}{2\Omega\eta} \right|_{z=0} \quad (29)$$

To understand how balance is achieved in the azimuthal vorticity equation (21), we need to include the effects of helium composition, via the mean molecular weight μ . Beneath the tachopause, gravitational settling produces an increase in μ , but within the confinement layer the persistent meridional circulation prevents any settling. We therefore replace \tilde{T} with $\tilde{T} - \tilde{\mu}$ in (1), where $\tilde{\mu}$ is the fractional departure of μ from its constant value in the confinement layer. The self-diffusivity of helium, $\chi \approx 10\text{cm}^2\text{s}^{-1}$, is negligible under our scaling assumptions, so the equation for the evolution of $\tilde{\mu}$ is simply

$$\frac{D\tilde{\mu}}{Dt} = 0. \quad (30)$$

We therefore anticipate a discontinuity in $\tilde{\mu}$ across the tachopause that balances the discontinuity in Coriolis and Lorentz force-curves in (21). This in fact requires the tachopause to have a slight Margules slope, which we verify in §10 is less than ϵ , and therefore negligible under our scaling assumptions for the confinement layer.

Beneath the tachopause, the combined thermal and compositional stratification ‘chokes’ any MMCs. We may therefore neglect \mathbf{u} in equations (13), (14) and (16). These equations together then imply $B_\phi \propto A_\phi$, so the toroidal and poloidal components of the field \mathbf{B} are closely related.

9.4 Boundary Conditions

It is not immediately clear how to choose well posed boundary conditions for the steady problem described by (21–27). In particular, the relationship between B_ϕ and A_ϕ described above means we can only impose *one* component of \mathbf{B} at the tachopause. We must therefore undertake a formal analysis of the system in order to choose appropriate boundary conditions. We take as our domain a cylinder of height H and radius R . The base $z = 0$ then corresponds to the tachopause and the top $z = H$ represents the upper extent of the confinement layer, located somewhere in the upper tachocline. The

outer surface $r = R$ is merely conceptual, and will generally be taken as 350Mm, corresponding to the colatitude at which the rotation in the tachocline matches that of the radiative interior.

If we linearise (21–27) and reduce the system to a single equation, then the highest order derivatives are found to be

$$\frac{\partial^4}{\partial z^4} \left[4 \frac{\partial^4}{\partial z^4} + (\mathbf{B}_p \cdot \nabla)^4 \right] + B_r^2 u_r \frac{\partial^5}{\partial r^5}.$$

So to formulate a well-posed problem we must specify four boundary conditions on both the upper and lower boundaries of our domain and, provided u_r remains positive, two conditions on the outer boundary. (Any remaining freedom is required to ensure that the solution remains finite at the axis.)

We therefore choose to impose the following boundary conditions:

- $\mathbf{B} = 0$ at $z = H$ (two conditions)
- $u_z = -1$ at $z = H$ (uniform downwelling)
- \tilde{T} prescribed at $z = H$
- B_r prescribed at $z = 0$
- $u_z = 0$ at $z = 0$ (no penetration into the radiation zone)
- $u_r = -\Lambda u_\phi$ at $z = 0$ (from equation (28))
- $\frac{\partial \tilde{T}}{\partial z} = 0$ at $z = 0$ (fast heat diffusion across the tachopause)
- Maxwell stress, $B_r B_\phi$, prescribed at $r = R$
- Radial electrical current density, $[\nabla \times \mathbf{B}]_r = -\frac{\partial B_\phi}{\partial z}$, prescribed at $r = R$

9.5 The Leading Order Solution

At some radius the horizontal flow u_r may become negative, implying that u_z becomes positive. In this case boundary layer separation may be expected, allowing the interior field to escape into the tachocline. However, this will only occur at radii comparable to the horizontal scale $\eta/\epsilon U$; closer to the pole, horizontal variations in all quantities can be regarded as small. In fact, if we focus our attention on a region sufficiently close to the pole, then we may expand all our quantities as power series in r . Then, to leading order, the vertical components of \mathbf{u} and \mathbf{B} are independent of r , and the horizontal components are proportional to r . If we retain only these leading order terms then our equations become

$$2u'_\phi = \frac{\partial \tilde{T}}{\partial r} + \frac{1}{r}(B_\phi^2)' - B_z B_r'' \quad (31)$$

$$2u_r = \frac{2}{r} B_r B_\phi + B_z B'_\phi \quad (32)$$

$$\frac{2}{r} u_r + u'_z = 0 \quad (33)$$

$$0 = -u_r B_z + u_z B_r - B_r' \quad (34)$$

$$0 = B_z u'_\phi - u_z B'_\phi + B_\phi'' \quad (35)$$

$$\frac{2}{r} B_r + B'_z = 0 \quad (36)$$

$$u_z = \tilde{T}'' \quad (37)$$

where primes denote vertical derivatives. These equations remain consistent provided the $\frac{\partial \tilde{T}}{\partial r}$ term in (31) is small, so that u_z remains principally a function of z alone. As long as this condition is met, (31–37) may be regarded as ODEs that describe a ‘similarity solution’ to the confinement layer problem.

In fact, these ODEs form an under-determined set: we may choose the functional form of any one of the independent quantities and deduce the others. This functional freedom replaces the freedom we previously had in choosing outer boundary conditions. It proves convenient to use this freedom to choose the profile $u_z(z)$, since then we may solve (32–36) directly to determine the remaining components of \mathbf{u} and \mathbf{B} ; in the absence of intuition regarding the Maxwell stress profile through the confinement layer, this is an appropriate way to proceed. Then (31) and (37) together place a limit on the horizontal range over which the solution can apply. Thus the thermodynamic variables are decoupled from the leading order problem. In the limit of strong stratification ($N \rightarrow \infty$), equations (32–36) remain valid to arbitrary colatitude. Furthermore, we note that these equations would not change if we dropped the thin layer approximation: we may say that solutions of (32–36) are *exact* in the strongly stratified and low Rossby number limit.

Since (31–36) do not rely on the thin layer approximation, we may apply them to a semi-infinite domain, with $u_z(z)$ chosen so that $u_z \rightarrow -1$ as $z \rightarrow \infty$. Using (33) and (36) we then rewrite (31), (32), (34) and (35) as

$$\frac{1}{2r} \frac{\partial \tilde{T}}{\partial r} = \frac{u'_\phi}{r} - \frac{B_\phi B'_\phi}{r^2} - \frac{B_z B_z'''}{4} \quad (38)$$

$$\left(\frac{B_\phi}{B_z} \right)' = -\frac{r u'_z}{B_z^2} \quad (39)$$

$$B_z'' = -u'_z B_z + u_z B_z' \quad (40)$$

$$u'_\phi = \frac{u_z B'_\phi - B_\phi''}{B_z} \quad (41)$$

In the rigidly rotating region below the tachopause, we deduce from (40) that the field has the form

$$B_r = B_0 r \quad \text{and} \quad B_z = -2B_0 z \pm (2\Lambda)^{1/2}, \quad (42)$$

where B_0 is a constant that parametrises the interior field strength. This is in agreement with our assumption of an internal magnetic field whose poloidal component is roughly dipolar. We then deduce from (39) that $B_\phi \propto r B_z$ (this is in fact a special case of the result described in §9.3 that $B_\phi \propto A_\phi$).

Within the confinement layer, with a given $u_z(z)$, (40) is a second-order linear ODE for B_z , and can readily be solved subject to the conditions that $B_z' = -2B_0$ at $z = 0$ and $B_z \rightarrow 0$ as $z \rightarrow \infty$. In particular, this determines the value of Λ . We then find a particular solution for B_ϕ , say \hat{B}_ϕ , by integrating (39) down from $z = \infty$:

$$\frac{\hat{B}_\phi}{r} = B_z \int_z^\infty \frac{u'_z}{B_z^2} \quad (43)$$

and obtain a corresponding \hat{u}'_ϕ from (41)

$$\hat{u}'_\phi = \frac{u_z \hat{B}'_\phi - \hat{B}_\phi''}{B_z} \quad (44)$$

The general B_ϕ and u'_ϕ may then be written as

$$B_\phi = \hat{B}_\phi + \alpha r B_z \quad (45)$$

$$u'_\phi = \hat{u}'_\phi + \alpha r u'_z \quad (46)$$

for some constant α . We find u_ϕ by integrating (46), subject to (28). Thus

$$\frac{u_\phi}{r} = \frac{u'_z(0)}{B_z(0)^2} + \int_0^z \frac{\hat{u}'_\phi}{r} dz + \alpha u_z. \quad (47)$$

We have now met all our boundary conditions on \mathbf{u} and \mathbf{B} at both the top and base of our domain. To fix a value for α we must therefore apply some condition at the sides of the domain; following Occam's razor, we choose α so that the total Maxwell stress on the sides of the domain vanishes. The Coriolis

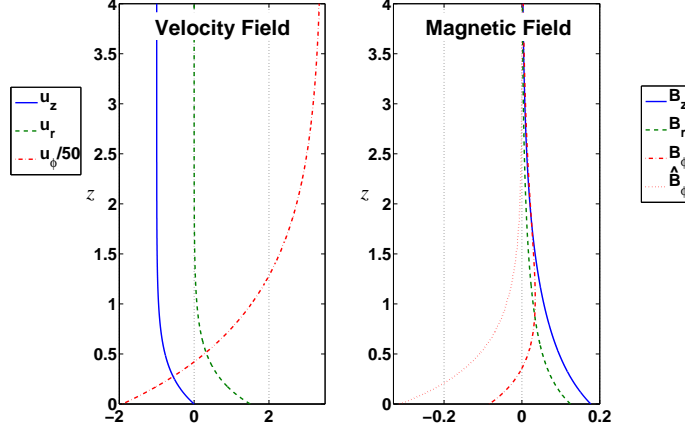


Figure 7: The velocity and magnetic field components for the solution with $u_z(z) = -(1 - e^{-3z})$, plotted at $r = \delta$. The large values of u_ϕ are explained in §9.7.

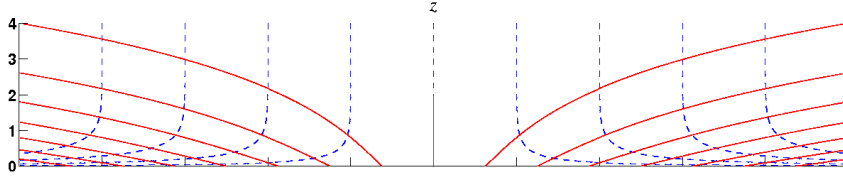


Figure 8: An elevation plot of the velocity streamlines (blue) and magnetic field lines (red) in the same solution, centred on the north pole.

torque produced by the flow through the confinement layer is therefore balanced entirely by the Maxwell torque at the tachopause. So we have

$$\int_0^\infty B_r B_\phi dz = 0. \quad (48)$$

But from (39) we find

$$B_r B_\phi = \frac{1}{2} [B_z B_\phi + r u_z]' \quad (49)$$

$$\therefore 0 = 2 \int_0^\infty B_r B_\phi dz = [B_z B_\phi + r u_z]_0^\infty \quad (50)$$

$$= -\alpha r B_z(0)^2 - B_z(0) \hat{B}_\phi(0) - r \quad (51)$$

$$\Rightarrow \alpha = -\frac{\frac{1}{r} B_z(0) \hat{B}_\phi(0) + 1}{B_z(0)^2} \quad (52)$$

Plots of the velocity and magnetic field profiles for a typical solution are shown in Figure 7. A vertical cross-section of the streamlines and field lines is shown in Figure 8.

9.6 Properties of the Solutions

The solution procedure described above is remarkably simple: with $u_z(z)$ given, the nonlinear equations can be solved as a series of linear ODEs. The solutions do not show sensitive dependence on the precise form of $u_z(z)$. Provided the chosen function $u_z(z)$ converges to -1 faster than e^{-2z} , the solutions derived above have $|\mathbf{B}_p| = O(e^{-z})$ as $z \rightarrow \infty$; then B_ϕ and $u'_\phi \rightarrow 0$ also, though not necessarily at the same rate. This disparity of scales, arising from the nonlinearity of the equations, has important implications for the numerical magnitudes of the various quantities. We return to this point in the next section.

If we suppose that the poloidal component of the Sun's internal field is roughly dipolar, and in particular antisymmetric between the north and south poles, then our solutions also have opposite signs

of B_ϕ between the two polar confinement layers. However, the internal toroidal field predicted in the numerical model of Braithwaite & Spruit [2] is roughly symmetric about the equatorial plane. Our similarity solutions cannot therefore hold throughout the entire solar interior; instead, there must be some torsional adjustment of the field within the radiation zone. This adjustment would have a similar structure to the torsional oscillations described in §7.

9.7 Scale Analysis

Our similarity solutions have two free parameters: the downwelling U and the interior field strength B_0 (we could alternatively take the height scale $\delta \equiv \eta/U$ and the Elsasser number $\Lambda \equiv \frac{B_z(0)^2}{2\Omega\eta}$ as our parameters). Restoring dimensions to all our variables (but keeping B_0 dimensionless), we find that the solutions conform to the scalings

$$\begin{aligned} u_z &\sim U \\ \frac{\partial}{\partial z} &\sim \frac{1}{\delta} \sim \frac{U}{\eta} \\ \frac{B_z}{\delta} &\sim \frac{B_r}{r} \sim \frac{(\Omega\eta)^{1/2}}{\delta} B_0 \\ \frac{u_r}{r} &\sim \frac{U}{\delta} \\ \Lambda &\sim \frac{B_z^2}{2\Omega\eta} \sim B_0^2 \\ \frac{u_\phi}{u_r} &\sim \frac{B_\phi}{B_r} \sim B_0^{-2} \\ \tilde{T} &\sim \frac{N^2\eta^2}{g\kappa U} \end{aligned}$$

The significance of the interior field strength arises from the azimuthal components of the momentum equation (22) and induction equation (25). In the ‘weak field’ case ($B_0 < 1$), differential rotation winds up the poloidal field lines, producing a strong toroidal component. This yields a prograde azimuthal Lorentz force of sufficient magnitude to gyroscopically pump the return flow of the MMC, preventing the downwelling from penetrating the radiation zone. In the ‘strong field’ case ($B_0 > 1$), the required pumping can be achieved with little winding up of the field lines. In both cases, the resulting poloidal–to–toroidal ratio of \mathbf{B} is of the order $O(B_0^{-2})$, so B_0^{-2} is a measure of the ‘spiralling’ of both the streamlines and the magnetic field lines. However, it can be seen from the plots in Figure 7 that the numerical factors hidden in these scalings are often significantly larger than unity. In particular, we commonly find

$$\frac{u'_r}{u'_\phi} \approx \frac{1}{2} B_0^2 \quad \text{and} \quad \frac{B'_r}{B'_\phi} \approx 20 B_0^2.$$

The reason for this is related to the ‘disparity of scales’ described earlier. The particular solution for B_ϕ defined by (43) decays to zero at a different rate than both B_r and B_z . This decay cannot be explained by advection–diffusion alone. In fact, it is due to the ‘winding up’ of poloidal field lines into toroidal field; in the steady state, this wind-up must occur rapidly enough to balance the diffusion of toroidal field up through the tachopause. Thus the principal balance in the toroidal induction equation (35) is

$$B''_\phi \approx -u'_\phi B_z. \quad (53)$$

The differential rotation in the confinement layer is therefore typically numerically larger than would be expected from scale analysis alone.

These large numerical factors have a bearing on the self-consistency of our analysis, though in the following sections we shall only perform a naïve check of our assumptions, based on the simple scalings above. A more careful check is carried out in [37] (although slightly different diffusion coefficients were used in that work).

9.7.1 Rossby Number, \mathcal{R}

To justify neglecting the nonlinear velocity terms in (32), we need the Rossby number \mathcal{R} number to be small, where

$$\mathcal{R} \equiv \frac{\frac{1}{r}(\mathbf{u} \cdot \nabla)(ru_\phi)}{2\Omega u_r} \sim \frac{U^2}{\Omega\eta} B_0^{-2} \quad (54)$$

So we need

$$\begin{aligned} \Leftrightarrow U &\ll (\Omega\eta)^{1/2} B_0 \\ \Leftrightarrow |\mathbf{u}| &\ll |\mathbf{B}| \end{aligned}$$

i.e. the confinement layer flow must be slower than the Alfvén speed.

9.7.2 Radius of validity

Our similarity solutions cease to apply when the $\frac{\partial \tilde{T}}{\partial r}$ term becomes significant in equation (12). Applying our scaling results, we find this occurs at the cylindrical radius $r = r_p$, where

$$r_p \sim \frac{N\eta^2}{(\Omega\kappa)^{1/2}U^2} \min(B_0, B_0^{-1}). \quad (55)$$

For given U , this radius is largest when $B_0 \approx 1$. For our solutions to be valid out to a given radius r_p , we then require

$$U \lesssim U_{max} \equiv \left(\frac{N^2\eta^4}{r_p^2\Omega\kappa} \right)^{1/4}. \quad (56)$$

For typical tachocline values of the parameters, and $r_p = 350\text{Mm}$ (corresponding roughly to 40° latitude), this upper limit is found to be $U_{max} \approx 2.5 \times 10^{-5} \text{cm s}^{-1}$, corresponding to a poloidal field at $r = r_p$ of approximately 70cm s^{-1} (i.e. 140G) and a Rossby number of around $\mathcal{R} \approx 6 \times 10^{-7}$.

9.7.3 Richardson Number, Ri_η

We have assumed throughout that the flow within the confinement layer is laminar. To justify this assumption, we need to check that the Richardson number is sufficiently large (i.e. that the shear is not able to overcome the stratification and produce Kelvin–Helmholtz instability). From the scalings derived above, we deduce

$$\begin{aligned} \text{Ri}_\eta^{-1} &\equiv \frac{1}{N^2} \left| \frac{\partial \mathbf{u}}{\partial z} \right|^2 \sim \frac{r^2 U^6}{N^2 \eta^4} \max(1, B_0^{-4}) \\ &\sim \mathcal{R} \frac{\eta r^2}{\kappa r_p^2} \end{aligned} \quad (57)$$

For typical solar parameters, the Roberts number $\kappa/\eta \approx 3 \times 10^4$, so this condition is easily satisfied even out to $r = r_p$, provided that the Rossby number is small. However, our confinement-layer solutions have a discontinuity in the horizontal velocity components at the tachopause, which we show in §10 is resolved over a Ekman layer of thickness $\delta_{Ek} \equiv \left(\frac{\nu}{2\Omega} \right)^{1/2}$. The Richardson number in this layer, Ri_ν , is therefore smaller by a factor δ_{Ek}^2/δ^2 , so

$$\begin{aligned} \text{Ri}_\nu &\sim \frac{\delta_{Ek}^2}{\delta^2} \text{Ri}_\eta \\ &\sim B_0^2 \frac{\kappa \nu r_p^2}{\eta^2 r^2} \end{aligned} \quad (58)$$

Thus at $r = r_p$, we find

$$\text{Ri}_\nu \sim \frac{\kappa \nu U^2}{\eta \Omega \eta \mathcal{R}}.$$

Since we already know that $U_{max} \ll \left(\frac{\Omega\eta^3}{\kappa\nu}\right)^{1/2} \approx 7 \times 10^{-4} \text{ cm s}^{-1}$, we have $\text{Ri}_\nu \ll 1/\mathcal{R}$. So shear stability within the Ekman layer is a stronger condition than low Rossby number.

In the limiting case described above, with $r_p = 350 \text{ Mm}$, $B_0 = 1$ and $U = 2.5 \times 10^{-5} \text{ cm s}^{-1}$, we find $\text{Ri}_\nu \approx 2200$. So the Ekman layer is Kelvin–Helmholtz stable in this case. In fact, the condition for shear stability in the Ekman layer, as seen from (58), is just

$$B_0 \gtrsim \left(\frac{\eta^2}{\kappa\nu}\right)^{1/2} \approx 1/50. \quad (59)$$

9.7.4 Tayler instability

As noted by Spruit [33], in stably stratified, differentially rotating fluids with magnetic fields, the first MHD instability to set in is typically the Tayler kink-type or ‘tipping’ instability. For a purely toroidal field in an unbounded cylindrical domain, within the Sun’s parameter regime, the condition for instability is just

$$\frac{d \ln B_\phi}{d \ln r} > -\frac{1}{2}$$

[33], which is certainly satisfied if $B_\phi \propto r$. In a system with a boundary at radius $r = R$, there is an additional condition:

$$\frac{B_\phi}{\Omega r} \gtrsim \left(\frac{N}{\Omega}\right)^{1/2} \left(\frac{\eta}{\kappa}\right)^{1/4} \left(\frac{\eta}{\Omega R^2}\right)^{1/4}$$

(see §A.4). This arises from the fact that the instability requires displacements that are ‘flat’ enough to overcome the strong stratification, yet ‘tall’ enough to evade magnetic diffusion.

In our model, with $B_\phi \propto r$ and the scalings derived above, this condition becomes

$$\frac{U^4}{B_0^4} \gtrsim \frac{N^2 \eta^4}{\Omega \kappa R^2} \equiv \frac{r_p^2}{R^2} U_{max}^4. \quad (60)$$

If we suppose that boundary layer separation occurs at $r \approx r_p$, then this is effectively the boundary of our domain. Setting $R = r_p$, we then find that the self-consistency condition implies Tayler stability for $B_0 > 1$. In cases with a strong toroidal field (i.e. $B_0 < 1$) condition (60) becomes more important, as we might expect from the nature of the instability.

9.8 Possible Parameter Ranges

Conditions (55), (59) and (60) can be summarised as follows:

$$U \lesssim U_{max} \min(B_0, B_0^{-1/2}) \quad (61)$$

$$B_0 \gtrsim \left(\frac{\eta^2}{\kappa\nu}\right)^{1/2} \approx 1/50 \quad (62)$$

with U_{max} defined as in (56). Under these conditions, the solutions described in §9.5 are valid for colatitudes up to 40° , and are free from both Tayler and Kelvin–Helmholtz instabilities. However, there is an additional condition on U : the downwelling must be sufficiently strong that the magnetic confinement layer is contained within the lower tachocline. This places a lower limit on U , say $U \lesssim U_{min}$. If we take $U_{min} = 2 \times 10^{-6} \text{ cm s}^{-1}$ then the confinement layer has height scale $\delta \lesssim 2 \text{ Mm}$. Combined with (61), this is a stronger condition than (62), and defines a ‘topological triangle’ in phase space within which our solutions are valid. The three limiting cases are

- $U = U_{max} \approx 2.5 \times 10^{-5} \text{ cm s}^{-1}$, $B_0 \approx 1$ (described earlier)
- $U = U_{min} \approx 2.0 \times 10^{-6} \text{ cm s}^{-1}$, $B_0 = U_{min}/U_{max} \approx 0.1$
- $U = U_{min} \approx 2.0 \times 10^{-6} \text{ cm s}^{-1}$, $B_0 = U_{max}^2/U_{min}^2 \approx 150$

The upper limit on poloidal field strength at $r = r_p$ is therefore

$$\begin{aligned} \frac{U_{max}^2}{U_{min}^2} \frac{U_{min}}{\eta} (\Omega\eta)^{1/2} r_p &\sim \left(\frac{\eta}{\kappa}\right)^{1/2} \frac{N\eta}{U_{min}} \\ &\approx 900 \text{cm s}^{-1} \text{ (or 1800G)}. \end{aligned}$$

So the largest internal field that can be confined by a confinement layer of thickness δ is

$$|\mathbf{B}| \lesssim (\eta/\kappa)^{1/2} N\delta. \quad (63)$$

10 The Tachopause

Though the tachopause was treated as a Margules front in §9.3, in fact the discontinuities in \mathbf{u} and $\tilde{\mu}$ will be resolved over a double boundary layer, with vertical scalings depending on viscosity, ν , and helium self-diffusivity, χ . Because of the importance of viscosity in the vorticity balance, we cannot use the Margules formula (81) to determine the slope of the tachopause. Instead, we include viscous terms in (21) and (22), and put helium diffusion on the RHS of (30). Under the scalings previously used for the confinement layer, we then obtain the equations

$$2\frac{\partial u_\phi}{\partial z} = \frac{\partial(\tilde{T} - \tilde{\mu})}{\partial r} + \frac{1}{r} \frac{\partial}{\partial z}(B_\phi^2) + r\mathbf{B}_p \cdot \nabla \left[\frac{1}{r} \frac{\partial^2}{\partial z^2} A_\phi \right] - 2\frac{\delta_{Ek}^2}{\delta^2} \frac{\partial^3 u_r}{\partial z^3} \quad (64)$$

$$2u_r = \frac{1}{r} \mathbf{B}_p \cdot \nabla(rB_\phi) + 2\frac{\delta_{Ek}^2}{\delta^2} \frac{\partial^2 u_\phi}{\partial z^2} \quad (65)$$

$$\mathbf{u}_p \cdot \nabla \tilde{\mu} = \frac{\chi}{\eta} \frac{\partial^2 \tilde{\mu}}{\partial z^2} \quad (66)$$

where

$$\delta = \eta/U \quad (67)$$

$$\delta_{Ek} = (\nu/2\Omega)^{1/2} \approx 20\text{m}. \quad (68)$$

So the jump in helium composition is resolved over a layer that is thinner than the magnetic confinement layer by a factor $(\chi/\eta)^{1/2} \approx 1/7$. The tachopause inherits the horizontal length scale of the overlying confinement layer, producing a tachopause slope of order $\epsilon(\chi/\eta)^{1/2}$, where ϵ is the slope of the confinement layer. The discontinuity in the horizontal flow is resolved over a much thinner Ekman layer of thickness $\delta_{Ek} \approx 20\text{m}$.

To maintain the small tilt of the tachopause, the variation in $\tilde{\mu}$ across the tachopause must be larger than the characteristic scale of \tilde{T} by a factor $(\eta/\chi)^{1/2}$, and so

$$\tilde{\mu} \sim \frac{N^2\eta^2}{g\kappa U} (\eta/\chi)^{1/2}. \quad (69)$$

Even in the case of weak downwelling, $U \approx 2 \times 10^{-6} \text{cm s}^{-1}$, this yields a fractional change in composition of only $\approx 5 \times 10^{-7}$, a tiny fraction of the compositional variation in the helium settling layer below [6].

11 The Tayler–Spruit Scenario

So far, we've not addressed precisely what mechanism generates the MMC within the tachocline. Due to the persistent differential rotation within the convection zone, any mechanism that opposes this shear will persistently drive such a circulation, as described in §5. Whilst microscopic kinematic viscosity within the tachocline is too small to be significant, the small scales produced by turbulent eddies might lead to enhanced dissipation, characterised by a larger 'eddy viscosity' that opposes the shear. To decide whether this mechanism can produce a circulation of the required magnitude, we need to decide what kind of turbulence can be present within the tachocline. As discussed previously, any turbulence

within the stably stratified tachocline must be predominantly horizontal, but since purely hydrodynamic horizontal turbulence has the ‘anti-frictional’ properties described in §6, it cannot produce the MMC required to confine the Sun’s interior magnetic field. It is therefore natural to ask what kinds of magnetohydrodynamic turbulence can exist within a sheared, rotating, stably stratified system.

A possible candidate for a turbulent tachocline dynamo was proposed by Spruit [34], and later identified in numerical simulations by Braithwaite & Spruit [3]. They recognised that the strong vertical shear within the tachocline would wind up any putative magnetic field to produce a large toroidal component. As described in §9.7.4, the first instability mechanism to arise would then be the Tayler kink-type or ‘tipping’ instability, which occurs in thermally stratified, rotating systems provided thermal diffusion is able to overcome the stratification constraint. This instability regenerates poloidal field, closing the dynamo loop (see §A.5). The dynamo saturates when the growth rate of the instability matches the timescale associated with the vertical shear, which requires the shear to exceed a critical value, given by (125). Since the dynamo is driven by the imposed shear, it is reasonable to expect a back reaction from the turbulence analogous to a viscosity. Spruit gives a scaling argument for the effective Maxwell stress produced by the turbulence, based on the nature of the Tayler instability. Remarkably, the effective viscosity, ν_e , is independent of both position and shear, provided the dynamo is operating continuously. Though the turbulent eddies are constrained to be nearly horizontal, magnetic diffusion stabilises the system on the smallest vertical scales, so we expect the turbulence to vanish at the bottom of the tachocline. We therefore characterise the effect of the Tayler–Spruit dynamo by a viscosity $\nu_e(z)$ that vanishes at the tachopause and tends to a constant above, given by Spruit’s estimate (122). To incorporate the effects of this effective viscosity within our equations, we simply replace the Lorentz terms on the RHS of (1) with the divergence of the viscous stress tensor, which is $(\nu_e(z)u_{i,j})_{,j}$ in suffix notation. If we consider only the effects of vertical differential rotation, then equation (11) becomes

$$2\Omega \frac{u_r}{r} = \frac{d}{dz} \left(\nu_e \frac{d}{dz} \left(\frac{u_\phi}{r} \right) \right). \quad (70)$$

Using mass conservation (2) we may then calculate the downwelling produced by the Tayler–Spruit dynamo by integrating (70) across the tachocline:

$$\begin{aligned} -\frac{\partial u_z}{\partial z} &= \frac{1}{r} \frac{\partial}{\partial r} (r u_r) \\ &= \frac{1}{\Omega} \frac{d}{dz} \left(\nu_e \frac{d}{dz} \left(\frac{u_\phi}{r} \right) \right) \end{aligned} \quad (71)$$

$$\Rightarrow U \sim \frac{\nu_e}{\Omega r} \frac{du_\phi}{dz} \quad (72)$$

If we suppose that the shear is close to its critical value (125), so that the dynamo is operating at threshold, then we estimate the downwelling produced to be

$$U^4 \sim \frac{N^2 \eta^4}{\Omega \kappa R^2} \quad (73)$$

As in 9.7.4, R is the horizontal ‘room’ available to the Tayler instability, which we might reasonably take to be the colatitude at which the magnetic confinement layer separates, r_p . But then (73) yields precisely the limiting value for the downwelling, U_{max} , found in §9.7.2. So the Tayler–Spruit dynamo, operating within the tachocline, could be responsible for generating the MMC that confines the interior field. In reality, the ‘back reaction’ from the dynamo on the shear in the tachocline might homogenise the differential rotation in that region; the dynamo would then shut off, allowing the shear to build up once more. Thus the dynamo would operate periodically in both space and time, producing a mean circulation weaker than U_{max} .

12 Concluding Remarks

We have seen how the Sun’s internal magnetic field can be confined, within the polar regions, by a persistent mean meridional circulation (MMC) within the tachocline. The field is confined within a ‘magnetic confinement layer’ whose thickness depends only on the magnitude of the MMC. The confinement will probably fail at some colatitude, allowing the internal field to upwell into the convection zone, where the Ferraro constraint demands that the angular velocity matches that of the interior.

Through helioseismology, we can estimate both the thickness of the confinement layer and the colatitude at which magnetic confinement fails. These estimates place reasonably tight constraints on the strength of the tachocline’s MMC, but permit a fairly wide range of interior field strengths ($\lesssim 2000\text{G}$).

A mechanism for producing the tachocline circulation might be the Tayler–Spruit dynamo [34], driven intermittently by vertical shear within the upper tachocline.

The ‘tachopause’, marking the lower extent of the tachocline, is held very nearly flat by the presence of a helium settling layer beneath, and presents a sharp, impermeable barrier to the MMC within the tachocline. The helium settling layer must therefore be in solid rotation throughout, perhaps down as far as $0.6R_\odot$. The low abundance of ${}^7\text{Li}$ observed in the Sun’s convection zone cannot therefore be the result of mixing between the convection zone and radiation zone whilst on the main sequence. Fortunately, other explanations for this low abundance exist [36]. In particular, a star of mass slightly over $1M_\odot$ would burn *all* its ${}^7\text{Li}$ before reaching the main sequence, and might then lose some mass through global pulsation. The Sun’s low ${}^7\text{Li}$ abundance could therefore be explained by a gradual *production* of ${}^7\text{Li}$ during its main sequence lifetime, perhaps by He–He collisions in hot solar flares.

13 Future Work

Though the simple similarity solutions presented in §9.5 offer much physical insight into the magnetic confinement problem, they provide only crude estimates for the scales of the various quantities. The model could be made quantitatively accurate by computing solutions to the full 2-d problem given by (21–27). In particular, this would determine if and where separation of the confinement layer occurs.

If the Sun’s ${}^7\text{Li}$ abundance cannot be explained by interior mixing, there are significant implications for stellar physics in general, since ${}^7\text{Li}$ abundance is often used to estimate the age of stars [19]. One way to test this hypothesis would therefore be to examine the correlation between stellar ${}^7\text{Li}$ abundance and other indicators of stellar age, such as X-ray luminosity [36].

14 Acknowledgements

I would like to thank both Michael McIntyre and Douglas Gough for their support and encouragement throughout this work. I am also indebted to Lee Anne Willson for an informative tutorial on the destruction and creation of ${}^7\text{Li}$ in stars.

A Appendix

A.1 Parameter Values

angular velocity	Ω	2.7×10^{-6}	s^{-1}
density	ρ	0.21	g cm^{-3}
pressure	p	6.7×10^{13}	$\text{g cm}^{-1}\text{s}^{-2}$
temperature	T	2.3×10^6	K
sound speed	c	2.3×10^7	cm s^{-1}
gravity	g	5.4×10^4	cm s^{-2}
density scale height	H_ρ	$0.12R_\odot$	
pressure scale height	H_p	$0.08R_\odot$	
adiabatic index	γ	1.665	
buoyancy frequency	N	8×10^{-4}	s^{-1}
magnetic diffusivity	η	4.1×10^2	cm^2s^{-1}
kinematic viscosity	ν	2.7×10^1	cm^2s^{-1}
thermal diffusivity	κ	1.4×10^7	cm^2s^{-1}
helium diffusion coefficient	χ	8.7	cm^2s^{-1}

All values are taken from [14].

A.2 The Perfect Gas Equations

In a frame rotating with angular velocity Ω , the equations governing a perfect gas are

$$\rho(\partial\mathbf{u}/\partial t + \mathbf{u} \cdot \nabla\mathbf{u} + 2\Omega \times \mathbf{u}) = -\nabla p + \rho\mathbf{g} + \mathbf{F} \quad (74)$$

$$\partial\rho/\partial t + \nabla \cdot (\rho\mathbf{u}) = 0 \quad (75)$$

$$p = \rho\mathcal{R}T \quad (76)$$

$$\rho T(\partial/\partial t + \mathbf{u} \cdot \nabla)s = F_D + \nabla \cdot (\rho c_p \kappa \nabla T) \quad (77)$$

We assume the specific heats c_v and c_p are constant and that the thermal diffusivity κ is also constant and isotropic. The gravitational acceleration \mathbf{g} includes a contribution from the centrifugal force, while \mathbf{F} incorporates Lorentz, viscous and imposed body forces. F_D represents viscous and Ohmic heating, and is neglected from here on since thermal heating is dominant in all cases to be studied. Finally, s is the specific entropy, given by

$$s = c_v \ln(p\rho^{-\gamma}) \quad (78)$$

where γ is the adiabatic index, $\gamma = c_p/c_v$.

A.2.1 The Taylor–Proudman Theorem

In many physical situations the dominant terms in the momentum equation (74) are the Coriolis, pressure and gravitational terms. If Ω and \mathbf{g} are both constant then the curl of (74) yields

$$\frac{\partial}{\partial t}(\nabla \times \mathbf{u}) + 2\Omega(\nabla \cdot \mathbf{u}_H) - (2\Omega \cdot \nabla)\mathbf{u}_H = \frac{1}{\rho^2}\nabla\rho \times \nabla p, \quad (79)$$

where a subscript H represents components perpendicular to Ω . So vorticity is generated by Coriolis shear and baroclinicity. For a barotropic fluid, the RHS of (79) vanishes, and the system only reaches a steady state when the contours of \mathbf{u}_H become aligned with the rotation axis.

A.2.2 Thermal Wind

In a baroclinic and axisymmetric fluid, only the azimuthal component on the RHS of (79) is non-zero. Therefore a steady state can be achieved in which axial variation of the rotation rate is balanced by

relative tilting of the density and pressure isopleths. Under the Boussinesq approximation, this balance may be expressed as

$$-(2\boldsymbol{\Omega} \cdot \nabla)\mathbf{u} = \mathbf{g} \times \nabla \tilde{T} \quad (80)$$

where \tilde{T} is the relative perturbation of temperature to a hydrostatic background. This is the ‘thermal wind’ balance in which vorticity production by Coriolis shear causes tilting of the stratification surfaces.

A particular case of thermal wind balance is the ‘Margules front’ in which both the angular velocity and the temperature perturbation are discontinuous across a sloped front. If we take $\boldsymbol{\Omega} = \Omega \mathbf{e}_z$ and $\mathbf{g} = -g \mathbf{e}_z$ then the slope of the front is given by the margules formula

$$-\frac{2\Omega}{g} \frac{\Delta u_\phi}{\Delta \tilde{T}} \quad (81)$$

A.3 Meridional Circulation and Spindown

A.3.1 Gyroscopic pumping

We take the perfect gas equations and linearise about a hydrostatic background, with $\mathbf{g} = -g \mathbf{e}_z$, in the frame rotating with angular velocity $\boldsymbol{\Omega} = \Omega \mathbf{e}_z$:

$$\frac{\partial}{\partial t}(\rho_0 \mathbf{u}) + 2\boldsymbol{\Omega} \times (\rho_0 \mathbf{u}) = -\nabla(\Delta p) + (\Delta \rho) \mathbf{g} + \mathbf{F} \quad (82)$$

$$\frac{\partial}{\partial t}(\Delta \rho) + \nabla \cdot (\rho_0 \mathbf{u}) = 0 \quad (83)$$

$$\frac{g}{c^2} \frac{\partial}{\partial t}(\Delta p) - \frac{\partial}{\partial t}(g \Delta \rho) + N^2(\rho_0 u_z) = \mathcal{Q}[\Delta \rho, \Delta p] \quad (84)$$

Here, $\Delta \rho$ and Δp are the departures of density and pressure from their background values, denoted by ρ_0 and p_0 , \mathbf{F} is a forcing term and \mathcal{Q} represents thermal relaxation, which may be taken to be a linear functional of the thermodynamic perturbations. The sound speed c and buoyancy frequency N are both functions of height z . We suppose that \mathbf{F} is a constant azimuthal force, i.e. $\mathbf{F} = F(\mathbf{x}) \mathbf{e}_\phi$, and average our equations over azimuth. Then the azimuthal component of (82) is

$$\frac{\partial}{\partial t}(\rho_0 u_\phi) + 2\Omega(\rho_0 u_r) = F, \quad (85)$$

so the forcing produces a meridional flow

$$\rho_0 u_r = F/2\Omega.$$

This is called ‘gyroscopic pumping’. For a retrograde force ($F < 0$), the resulting flow is poleward.

A.3.2 Downward control

If F is confined to some finite range in z (i.e. to a ‘forcing layer’) then the steady meridional flow described above must in fact be part of a mass-conserving meridional circulation. The ‘return flow’ of the circulation cannot be steady since there is nothing to balance its Coriolis force. The system therefore undergoes either spin-down or spin-up, depending on the sign of F .

The principle of ‘downward control’ states that, in a stably stratified atmosphere, the adjustment of the system in response to the forcing occurs *below* the level at which the forcing is applied. Thus the steady meridional flow described in the previous section represents the *top* of a meridional circulation. In particular, this means that a retrograde force leads to downward flux (i.e. downwelling) at the pole. The physical explanation of downward control is simple: since the density in a stratified atmosphere decreases exponentially with height, the kinetic energy associated with a flow of given mass flux *increases* exponentially with height. Energy dissipation within the system (represented by \mathcal{Q} in equation (84)) will therefore cause the return flow to spread downward rather than upward. This is called ‘radiative spreading’. We now derive the principle of downward control mathematically.

Because of the form of equations (82–84), we choose to take mass flux rather than fluid velocity as our basic variable. We therefore define

$$\tilde{\mathbf{u}} \equiv \rho_0 \mathbf{u}. \quad (86)$$

Following Haynes et al. [16] we assume hydrostatic and cyclostrophic balance, and therefore neglect the $\frac{\partial}{\partial t}$ terms in the poloidal components of (82). We also make the anelastic approximation, which means dropping the $\frac{\partial}{\partial t}$ term from (83). These idealisations filter out the effects of wave propagation, but make the system non-local and therefore sensitive to the choice of boundary conditions. However, under these assumptions the system contains only two independent variables, which we take to be \tilde{u}_z and Δp . We may then regard \mathcal{Q} as a functional of Δp only, and thus derive the following equation for the evolution of \tilde{u}_z :

$$\partial_t \mathcal{B} \tilde{u}_z + (\partial_t \mathcal{D} - \mathcal{Q}) \left(\partial_z \tilde{u}_z + \frac{1}{2\Omega r} \partial_r (rF) \right) = \frac{1}{4\Omega^2} [\partial_t \nabla_H^2, \mathcal{Q}] (\Delta p), \quad (87)$$

where the operators \mathcal{B} and \mathcal{D} are defined as

$$\mathcal{B} \equiv \frac{N^2}{4\Omega^2} \nabla_H^2 \quad (88)$$

$$\mathcal{D} \equiv \frac{\partial}{\partial z} + \frac{g}{c^2} \quad (89)$$

Here, $\nabla_H^2 \equiv \nabla^2 - \frac{\partial^2}{\partial z^2}$ is the horizontal Laplacian.

For natural choices of \mathcal{Q} , the commutator on the RHS of (87) vanishes, so we obtain a single equation relating the vertical mass flux \tilde{u}_z to the imposed forcing F . We now consider the evolution of a cylindrical domain, V , governed by equation (87). To study the effect of the forcing, we must choose boundary conditions that do not represent energy injection into the system. This is equivalent to choosing boundary conditions such that the total energy is non-increasing when $F \equiv 0$. But in that case (87) implies

$$\partial_t (\mathcal{B} + \mathcal{D} \partial_z) \tilde{u}_z = \mathcal{Q} \partial_z \tilde{u}_z \quad (90)$$

$$\Rightarrow \partial_t [(\mathcal{B} + \mathcal{D} \partial_z) \tilde{u}_z]^2 = 2 [(\mathcal{B} + \mathcal{D} \partial_z) \tilde{u}_z] [\mathcal{Q} \partial_z \tilde{u}_z] \quad (91)$$

$$\Rightarrow \frac{d}{dt} \int_V \frac{1}{2} [(\mathcal{B} + \mathcal{D} \partial_z) \tilde{u}_z]^2 dV = \int_V [(\mathcal{B} + \mathcal{D} \partial_z) \tilde{u}_z] [\mathcal{Q} \partial_z \tilde{u}_z] dV \quad (92)$$

So we must choose boundary conditions such that the RHS of (92) is negative definite.

We now restrict attention to the case of an isothermal background with Newtonian cooling. Then N and c are constant and

$$\mathcal{Q}[\Delta p] \equiv -\alpha g \frac{\rho_0}{T_0} (\Delta T) \quad (93)$$

$$\Rightarrow \mathcal{Q} \equiv -\alpha \left(\frac{\partial}{\partial z} + \frac{\gamma g}{c^2} \right) \quad (94)$$

where γ is the adiabatic index. In this case we find

$$-\frac{1}{\alpha} [\mathcal{D} \partial_z u] [\mathcal{Q} \partial_z u] = (\partial_z^2 u)^2 + \gamma \left(\frac{g \partial_z u}{c^2} \right)^2 + \left(\frac{(\gamma + 1)g}{2c^2} \right) \partial_z ((\partial_z u)^2)$$

and

$$-\frac{1}{\alpha} \frac{4\Omega^2}{N^2} [\mathcal{Q} \partial_z u] [\mathcal{B} u] = |\nabla_H \partial_z u|^2 - \frac{1}{\alpha} \nabla_H \cdot ((\tilde{\mathcal{Q}} \partial_z u) \nabla_H u) - \frac{1}{2} \partial_z^2 (|\nabla_H u|^2),$$

so

$$\begin{aligned} \frac{d}{dt} \int_V \frac{1}{2} [(\mathcal{B} + \mathcal{D} \partial_z) \tilde{u}_z]^2 dV &\leq \frac{\alpha}{2} \int \left(\left(\frac{(\gamma + 1)g}{c^2} \right) (\partial_z \tilde{u}_z)^2 - \frac{N^2}{4\Omega^2} \partial_z (\partial_r \tilde{u}_z)^2 \right) dS \\ &+ \frac{\alpha}{2} \int \frac{N^2}{4\Omega^2} \partial_z (\partial_r \tilde{u}_z)^2 dS \\ &+ \frac{N^2}{4\Omega^2} \int (\mathcal{Q} \partial_z \tilde{u}_z) (\partial_r \tilde{u}_z) dS \end{aligned} \quad (95)$$

the three surface integrals being taken respectively over the base, top and sides of the domain. So our boundary conditions must be that $\partial_z \tilde{u}_z = 0$ on the base, $(\partial_r \tilde{u}_z)(\partial_r \partial_z \tilde{u}_z) = 0$ on the top and $(\mathcal{Q} \partial_z \tilde{u}_z)(\partial_r \tilde{u}_z) = 0$ on the sides. However, this only ensures that the solution decays to a state with $\partial_z \tilde{u}_z = 0$ throughout; indeed, the governing equation (87) cannot predict the evolution of the system after this point. For the problem to be well posed, and to ensure that all solutions tend to zero when $F = 0$, we need to impose an extra boundary condition. The only such condition that is compatible with our existing boundary conditions is $\tilde{u}_z = 0$ on the top surface: any other choice would overspecify the problem, and it would then be possible to choose a forcing F such that there is no solution. This boundary condition also has a physical interpretation if the experiment is unbounded above: since the density decays exponentially with height, if \tilde{u}_z does not tend to zero as $z \rightarrow \infty$ then the kinetic energy diverges. So this boundary condition is necessary to prevent an infinite discontinuity in the energy of the system, which would be unphysical.

So we have the following boundary conditions on our domain:

- $\partial_z \tilde{u}_z = 0$ on the base
- $\tilde{u}_z = 0$ on the top
- $(\mathcal{Q} \partial_z \tilde{u}_z)(\partial_r \tilde{u}_z) = 0$ on the sides

Together these guarantee that all initial conditions decay to zero when there is no forcing. More generally, they guarantee that all solutions for a given F converge, so the long-time behaviour of solutions is independent of their initial conditions. But since F is time-independent, one solution of (87) is just

$$\tilde{u}_z = \frac{1}{2\Omega} \int_z^\infty \frac{1}{r} \partial_r(rF) dz, \quad (96)$$

which vanishes above the ‘forcing layer’ in which F is non-zero. So any disturbance above the forcing layer is just a transient, and vanishes after sufficient time. Thus the meridional flow produced by the imposed forcing is confined entirely below the forcing layer: this is downward control.

In fact, the solution described by (96) is not quite a meridional circulation, since it simply represents constant vertical mass flux through each horizontal surface below the forcing layer. To produce a circulation, we would need to impose no-penetration boundary conditions on the base and sides of the domain. The steady state of the system is then

$$\tilde{u}_z = \frac{1}{2\Omega} \int_z^\infty \frac{1}{r} \partial_r(rF) dz - \frac{1}{2\Omega} \exp(-\frac{\gamma g}{c^2} z) \int_0^\infty \frac{1}{r} \partial_r(rF) dz. \quad (97)$$

So the vertical mass flux decays exponentially at the same rate as the background density.

A.3.3 The hydrodynamic tachocline model

We can reproduce the tachocline model of Spiegel & Zahn [32] by taking the Boussinesq ($c \rightarrow \infty$) limit of equation (87) and choosing

$$\mathcal{Q}[\Delta p] \equiv \kappa g \frac{\rho_0}{T_0} \nabla^2(\Delta T) \quad (98)$$

$$\Rightarrow \mathcal{Q} \equiv \kappa \nabla^2 \frac{\partial}{\partial z} \quad (99)$$

If $F \equiv 0$ then we obtain the evolution equation

$$\partial_t \left(\frac{N^2}{4\Omega^2} \nabla_H^2 + \partial_z^2 \right) \tilde{u}_z = \kappa \nabla^2 \partial_z^2 \tilde{u}_z. \quad (100)$$

Though we have chosen to use \tilde{u}_z as our basic variable, we could equivalently have chosen \tilde{u}_ϕ , in which case we would have obtained the equation

$$\partial_t \left(\frac{N^2}{4\Omega^2} (\nabla_H^2 - \frac{1}{r^2}) + \partial_z^2 \right) \tilde{u}_\phi = \kappa \nabla^2 \partial_z^2 \tilde{u}_\phi, \quad (101)$$

the additional term arising from the geometry of the problem. Spiegel & Zahn considered the effect of imposing an inhomogeneous boundary condition in \tilde{u}_ϕ at the top of the domain, chosen to represent the nonuniform rotation in the lower convection zone. Since noted that the ratio $\frac{N^2}{4\Omega^2}$ is very large within the tachocline (around 3×10^4), the system then quickly attains a state in which $|\partial_z^2 \tilde{u}_\phi| \ll |\frac{N^2}{4\Omega^2} \nabla_H^2 \tilde{u}_\phi|$; this occurs on a timescale κ/Δ^2 , where Δ is the thickness of the tachocline. However, the typical vertical scale, Δ , remains much larger than the imposed horizontal scale, say l . After this point the evolution of the system may therefore be approximated by the equation

$$\frac{N^2}{4\Omega^2} \partial_t (\nabla_H^2 - \frac{1}{r^2}) \tilde{u}_\phi = \kappa \partial_z^4 \tilde{u}_\phi. \quad (102)$$

This is the inviscid analogue of equation (4.10) in [32]. So the imposed horizontal variation of \tilde{u}_ϕ spreads into the tachocline, causing the effective tachocline thickness to increase on a timescale

$$1/t \sim \frac{4\Omega^2 l^2 \kappa}{N^2 \Delta^2 \Delta^2} \quad (103)$$

$$\Rightarrow \Delta \sim l(t/t_{ES})^{1/4} \quad (104)$$

$$\text{where } t_{ES} \equiv \frac{N^2 l^2}{4\Omega^2 \kappa} \quad (105)$$

As noted in [32], the characteristic timescale of the spreading is the local Eddington–Sweet time, which is around 10^{11} years. Due to the 1/4 power in (104), the time taken for Δ to become comparable to l is only a small fraction of t_{ES} . Spiegel & Zahn therefore concluded that over the 4.6×10^9 years of the Sun’s main-sequence lifetime, the tachocline’s thickness should have become a significant fraction of the Sun’s radius.

A.4 The Tayler Instability

We take equations (1–5) and linearise about a constant background field, so $\mathbf{B}(\mathbf{x}, t) \rightarrow \mathbf{B}(\mathbf{x}) + \mathbf{b}(\mathbf{x}, t)$. Hence

$$\frac{\partial \mathbf{u}}{\partial t} + 2\boldsymbol{\Omega} \times \mathbf{u} = -a^2 \nabla \tilde{p} + \vartheta \mathbf{e}_z + (\nabla \times \mathbf{B}) \times \mathbf{b} + (\nabla \times \mathbf{b}) \times \mathbf{B} \quad (106)$$

$$\nabla \cdot \mathbf{u} = 0 \quad (107)$$

$$\frac{\partial \mathbf{b}}{\partial t} = \mathbf{B} \cdot \nabla \mathbf{u} + \mathbf{u} \cdot \nabla \mathbf{B} + \eta \nabla^2 \mathbf{b} \quad (108)$$

$$\nabla \cdot \mathbf{b} = 0 \quad (109)$$

$$\frac{\partial \vartheta}{\partial t} + N^2 u_z = \kappa \nabla^2 \vartheta \quad (110)$$

We suppose that $\mathbf{B} = B \mathbf{e}_\phi$, where the Alfvén frequency $\omega_A \equiv B/r$ is constant (and $\ll \Omega$), and that all perturbed quantities are proportional to $\exp(inz + im\phi - i\omega t)$. We are interested in instabilities of the magnetic field, which we anticipate will grow on timescales no faster than ω_A . We may therefore ignore the effect of inertial waves, which have a timescale given by 2Ω ; this corresponds to neglecting the time derivative in (106). We also make the thin layer approximation: “ $\nabla^2 \equiv \nabla_H^2 + \frac{\partial^2}{\partial z^2} \approx \frac{\partial^2}{\partial z^2}$ ”. We may then combine all our linear equations into a single equation for b_z :

$$(\nabla_H^2 + L^2) b_z = 0, \quad (111)$$

$$\text{where } L^2 = \frac{n^2 \omega_A^2 \omega + in^2 \kappa}{N^2 \omega + in^2 \eta} \left[4 \left(1 + \frac{\Omega}{m \omega_A^2} (\omega + in^2 \eta) \right)^2 - m^2 \right]. \quad (112)$$

Far from the pole, where $\nabla_H^2 \approx \frac{\partial^2}{\partial r^2}$, we recover the same result as equation (A18) of [33], in the particular case where $B \propto r$. In the limit $\kappa/\eta \gg 1$, we seek unstable modes with $|\omega| \ll n^2 \kappa$. If there is

no lower bound on L then we may take n to be arbitrarily small, and thus consider only frequencies in the range $n^2\eta \ll \omega \ll n^2\kappa$. Then (112) becomes

$$\frac{L^2}{n^4} = \frac{\omega_A^2}{N^2} \frac{i\kappa}{\omega} \left[4 \left(1 + \frac{\Omega\omega}{m\omega_A^2} \right)^2 - m^2 \right]. \quad (113)$$

and there are unstable modes for $m = 1$ and $\text{Re}(\hat{\omega}) \in (-\frac{1}{2}, 0)$, where $\hat{\omega} \equiv \frac{\Omega}{\omega_A^2}\omega$. We see from (113) that these modes have

$$L^2 \sim \frac{\Omega\kappa}{N^2} n^4.$$

If there is some lower bound on L , say $L \leq L_0$, then we can no longer take $n^2\eta \ll \omega$. Instead, we seek the maximum marginally stable horizontal wavenumber, i.e. we maximise (112) over $\hat{\omega} \in (-\frac{1}{2}, 0)$. We then find that unstable modes exist iff

$$L_0^2 < L_{max}^2 \equiv \frac{8\omega_A^4\kappa}{N^2\Omega\eta^2} \max_{\hat{\omega} \in (-1/2, 0)} \left\{ (-\hat{\omega})^{1/2} (1 + \hat{\omega}) \left[\frac{(1 + \hat{\omega})^2 - 1/4}{2 + \hat{\omega}} \right]^{3/2} \right\} \quad (114)$$

$$\sim \frac{\omega_A^4\kappa}{N^2\Omega\eta^2} \quad (115)$$

$$\Leftrightarrow \omega_A^4 \gtrsim N^2\Omega\eta \frac{\eta}{\kappa} L_0^2 \quad (116)$$

and all unstable modes have growth rate $\omega \sim \omega_A^2/\Omega$.

A.5 The Tayler–Spruit Dynamo

Suppose we have a cylinder of stably stratified, rotating fluid, threaded by a weak, approximately homogeneous magnetic field. If we impose vertical differential rotation of the form

$$\frac{u_\phi}{r} = \frac{u_\phi}{r}(z),$$

then any vertical component of the field is wound into a toroidal component according to the induction equation

$$\frac{\partial}{\partial t} \omega_A \sim B_z \frac{d}{dz} \frac{u_\phi}{r},$$

where

$$\omega_A \equiv \frac{B_\phi}{r}.$$

Once the toroidal field becomes sufficiently large, it is subject to the Tayler instability, which regenerates a vertical field component on a timescale Ω/ω_A^2 (see §A.4). The criterion for instability is

$$\omega_A^4 \gtrsim \frac{N^2}{\kappa R^2} \Omega \eta^2 \quad (117)$$

where R is the radius of the cylinder (see equation (116)). Since the protofield was independent of r , so is ω_A , and the instability threshold is therefore breached throughout the entire domain at the same instant. In order for the dynamo to saturate, the growth rate of the instability must match the wind-up rate of poloidal field, i.e.

$$\frac{\omega_A^2}{\Omega} \sim \frac{B_z}{\omega_A} \frac{d}{dz} \frac{u_\phi}{r}. \quad (118)$$

The Maxwell stresses produced by the dynamo may be characterised by a viscosity ν_e , where

$$\nu_e \frac{\partial}{\partial z} u_\phi \sim B_z B_\phi \quad (119)$$

$$\Rightarrow \nu_e \sim \Omega \frac{B_z^2}{\omega_A^2}, \quad (120)$$

which we note is independent of r . Following Spruit [34], we suppose that the structure of the dynamo field is determined by the nature of the Tayler instability, and so $B_\phi/B_z \sim nr$, where n is the vertical wavenumber of the most unstable mode. At the instability threshold, the only unstable vertical wavenumber is given by

$$n^4 \sim \frac{N^2}{\Omega\kappa R^2}. \quad (121)$$

For larger ω_A , the most unstable wavenumber is only weakly dependent on ω_A , so the effective eddy viscosity is

$$\nu_e \sim \frac{\Omega}{N} R (\Omega\kappa)^{1/2}. \quad (122)$$

If we also set $B_\phi/B_z \sim nr$ in (118), with n given by (121), then we find

$$\frac{\omega_A^2}{\Omega} \sim \frac{1}{n} \frac{d}{dz} \frac{u_\phi}{r} \quad (123)$$

$$\Rightarrow \omega_A^4 \sim \frac{\Omega^2 R}{N} (\Omega\kappa)^{1/2} \left(\frac{d}{dz} \frac{u_\phi}{r} \right)^2 \quad (124)$$

which provides an estimate of the toroidal field that can be maintained by the vertical shear. For the dynamo to be operating continuously, this must exceed the critical value given by (117), so

$$\frac{d}{dz} \frac{u_\phi}{r} \gtrsim \eta \left(\frac{N^2}{\Omega\kappa R^2} \right)^{3/4}. \quad (125)$$

References

- [1] Acheson D. J., 1978, *PTRSL*, **A 289**, 459
- [2] Braithwaite J. & Spruit H. C., 2004, *Nature*, **431**, L819
- [3] Braithwaite J. & Spruit H. C., 2006, *A&A* (submitted)
- [4] Brun A. S. & Toomre J., 2002, *ApJ*, **570**, 865
- [5] Brun A. S. & Zahn J.-P., 2006, *A&A*, **457**, 665
- [6] Ciaccio F., Degl’Innocenti S., Ricci B., 1997, *A&A*, **123**, 449
- [7] Cowling T.G., 1957 *Magnetohydrodynamics*, Interscience, New York
- [8] Einstein A., 1934, in *Essays in Science*, 85–91. New York: Philosophical Library
- [9] Ferraro V. C. A., 1937, *MNRAS*, **97**, 458
- [10] Garaud P., 2002, *MNRAS*, **329**, 1
- [11] Garaud P., 2007, in *The Solar Tachocline*, ed. Hughes D. W., Rosner R., Weiss N. O. Cambridge University Press, Cambridge
- [12] Gilman P. A. & Miller J., 1981, *ApJS*, **46**, 211
- [13] Gough D. O., 1969, *JAS*, **26**, 448
- [14] Gough D. O., 2007, in *The Solar Tachocline*, ed. Hughes D. W., Rosner R., Weiss N. O. Cambridge University Press, Cambridge

- [15] Gough D. O. & McIntyre M. E., 1998, *Nature*, **394**, 755
- [16] Haynes P. H. et al., 1991, *JAS*, **48**, 651
- [17] Holton J.R., 1965, *JAS*, **22**, 402
- [18] MacGregor K. B. & Charbonneau P., 1999, *ApJ*, **519**, 911
- [19] Mazzitelli I., 1990, in *Rotation and Mixing in Stellar Interiors*, ed. Goupil M.-J., & Zahn J.-P., Springer, Heidelberg
- [20] McIntyre M. E., 1994, in *The Solar Engine and its Influence on the Terrestrial Atmosphere and Climate* (Vol. 25 of NATO ASI Subseries I, Global Environmental Change), ed. E. Nesme-Ribes. Springer-Verlag, Heidelberg
- [21] McIntyre, M. E., 2003. in *Stellar Astrophysical Fluid Dynamics*, ed. M.J. Thompson & J. Christensen-Dalsgaard. Cambridge, University Press, 111–130.
- [22] McIntyre M. E., 2007, in *The Solar Tachocline*, ed. Hughes D. W., Rosner R., Weiss N. O. Cambridge University Press, Cambridge
- [23] Mestel L. & Moss D., 1986, *MNRAS*, **221**, 25
- [24] Mestel L. & Weiss N. O., 1987, *MNRAS*, **226**, 123
- [25] Miesch M. S., Brun A. S. & Toomre J., 2005, *ApJ*, **641**, 618
- [26] Mitra-Kraev U. & Thompson M. J., 2007, *AstNach*, **328**, No.10, 1009
- [27] Prendergast K.H., 1956, *ApJ*, **123**, 498
- [28] Rädler K.-H., 1986, in *Plasma Astrophysics*, Proceedings Joint Varenna–Abastumani Workshop, ESA
- [29] Rüdiger G., 1989, *Differential Rotation and Stellar Convection*, Gordon and Breach, New York
- [30] Rüdiger G. & Kitchatinov L. L., 1997, *AsN*, **318**, 273
- [31] Spiegel E. A., 1972, in *Physics of the Solar System*, ed. Rasool S. I. NASA, SP-300, 61
- [32] Spiegel E. A. & Zahn J.-P., 1992, *A&A*, **265**, 106
- [33] Spruit H. C., 1999, *A&A*, **349**, 189
- [34] Spruit H. C., 2002, *A&A*, **381**, 923
- [35] Walén C., 1946, *AMAF*, **30A**, no. 15
- [36] Willson L. A., private communication
- [37] Wood T. S. & McIntyre M. E., 2007, in *Unsolved Problems in Stellar Physics*, University Press, Cambridge